



<b>Publication Year</b>	2019
<b>Acceptance in OA @INAF</b>	2020-11-25T15:12:43Z
<b>Title</b>	H3+ characteristics in the Jupiter atmosphere as observed at limb with Juno/JIRAM
<b>Authors</b>	MIGLIORINI, Alessandra; Dinelli, B. M.; Moriconi, M. L.; ALTIERI, FRANCESCA; ADRIANI, Alberto; et al.
<b>DOI</b>	10.1016/j.icarus.2019.04.003
<b>Handle</b>	<a href="http://hdl.handle.net/20.500.12386/28549">http://hdl.handle.net/20.500.12386/28549</a>
<b>Journal</b>	ICARUS
<b>Number</b>	329

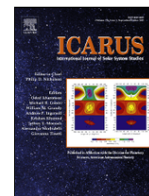


ELSEVIER

Contents lists available at ScienceDirect

Icarus

journal homepage: www.elsevier.com



## $H_3^+$ characteristics in the Jupiter atmosphere as observed at limb with Juno/JIRAM

A. Migliorini<sup>a, \*</sup>, B.M. Dinelli<sup>b</sup>, M.L. Moriconi<sup>c</sup>, F. Altieri<sup>a</sup>, A. Adriani<sup>a</sup>, A. Mura<sup>a</sup>, J.E.P. Connerney<sup>d, e</sup>, S.K. Atreya<sup>f</sup>, G. Piccioni<sup>a</sup>, F. Tosi<sup>a</sup>, G. Sindoni<sup>g</sup>, D. Grassi<sup>a</sup>, S.J. Bolton<sup>h</sup>, S.M. Levin<sup>i</sup>, J.-C. Gérard<sup>j</sup>, R. Noschese<sup>a</sup>, A. Cicchetti<sup>a</sup>, R. Sordini<sup>a</sup>, A. Olivieri<sup>g</sup>, C. Plainaki<sup>g</sup>

<sup>a</sup> INAF-IAPS, Istituto di Astrofisica e Planetologia Spaziali, 00133 Rome, Italy

<sup>b</sup> ISAC-CNR, via Gobetti, 101, Bologna, Italy

<sup>c</sup> ISAC-CNR, via Fosso del Cavaliere, 100, Roma, Italy

<sup>d</sup> Space Research Corporation, Annapolis, MD, USA

<sup>e</sup> NASA Goddard Space Flight Center, Greenbelt, MD, USA

<sup>f</sup> Planetary Science Laboratory, University of Michigan, Ann Arbor, MI, USA

<sup>g</sup> Agenzia Spaziale Italiana, Rome, Italy

<sup>h</sup> Southwest Research Institute, San Antonio, TX, USA

<sup>i</sup> Jet Propulsion Laboratory, University of Iowa, Iowa City, IA, USA

<sup>j</sup> Laboratoire de Physique Atmosphérique et Planétaire, Université de Liège, Liège, Belgium

### ARTICLE INFO

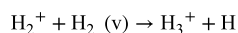
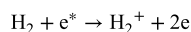
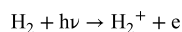
### ABSTRACT

NASA's Juno spacecraft has been orbiting Jupiter since August 2016, providing unprecedented insights into the giant planet's atmosphere. The Jupiter Infrared Auroral Mapper (JIRAM) experiment on board Juno has made spectroscopic observations of the trihydrogen cation ( $H_3^+$ ) emissions in both northern and southern auroral regions (Dinelli et al., 2017; Adriani et al., 2017; Mura et al., 2017) and at mid-to-low latitudes (this paper). Observations targeting the limb of the planet from  $60^\circ$  North to  $60^\circ$  South latitudes were acquired with JIRAM's spectrometer in August 2016 and March 2017. We use these observations to characterize, for the first time, the vertical distribution of the  $H_3^+$  emissions as a function of latitude across Jupiter's dayside.  $H_3^+$  emission features in the  $3\text{--}4\ \mu\text{m}$  spectral band were used to retrieve the  $H_3^+$  volume mixing ratio (VMR) and atmospheric temperatures as a function of altitude. The  $H_3^+$  density profile has a quasi-symmetric distribution with latitude, decreasing from  $5 \times 10^4\ \text{cm}^{-3}$  at 300 km to  $2 \times 10^3\ \text{cm}^{-3}$  at 650 km altitude above the 1-bar level (column densities of  $3.5 \times 10^{12}\ \text{cm}^{-2}$  to  $1.4 \times 10^{11}\ \text{cm}^{-2}$ , assuming a 700 km column depth). The  $H_3^+$  VMR is higher in the Southern hemisphere than in the North with values at 500 km of  $\sim 4 \times 10^{-4}$  ppmv at  $40^\circ\text{N}$  and  $\sim 8 \times 10^{-4}$  ppmv at  $40^\circ\text{S}$ . Retrieved temperatures increase almost monotonically with increasing altitude, hovering around 400 K at 300 km and  $>900$  K at about 700 km.

### 1. Introduction

$H_3^+$  is a key ion in Jupiter's upper atmosphere, where its emissions at infrared wavelengths reveal energy deposition in Jupiter's polar regions (Connerney and Satoh, 2000). It is thus a valuable diagnostic of Jovian auroral processes and satellite interactions that deposit energy in Jupiter's upper atmosphere (Connerney et al., 1993; Clarke et al., 2002; Mura et al., 2017; Mura et al., 2018; Gérard et al., 2018).  $H_3^+$  infrared emissions were observed also at non-auroral latitudes (Miller et al., 1997; Ballester et al., 1994; Stallard et al., 2015) both from space and ground-based telescopes.  $H_3^+$  is produced (e.g., Miller et al., 2000)

in Jupiter's ionosphere by chemical reactions, such as:



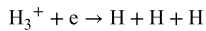
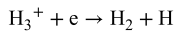
where  $h\nu$  is the solar extreme ultraviolet radiation (indicating photoionization) and  $e^*$  represents electrons energetic enough to produce further ionization. At polar latitudes, electron impact ionization is the dominant ionization pathway, whereas photoionization may be ex-

\* Corresponding author.

Email address: alessandra.migliorini@iaps.inaf.it (A. Migliorini)

pected to contribute to a much lesser extent across the illuminated disc of the planet.

$\text{H}_3^+$  is removed by dissociative recombination of  $\text{H}_3^+$ , for example:



but it is also vulnerable to loss via charge exchange with minor species (for example,  $\text{H}_2\text{O}$ ) which plays an important role in Saturn's ionosphere (Connerney and Waite, 1984; Moses and Bass, 2000; Moore et al., 2015). Below the homopause, it quickly reacts with methane and its density drops to very low values. Even if  $\text{H}_3^+$  emissions have been observed at all latitudes on Jupiter, the lower latitude emission intensities are typically only a few percent of those associated with auroral emissions (Stallard et al., 2018). Several mechanisms have been invoked to explain the observed emissions at mid-to-low latitudes on the night-side of Jupiter (Stallard et al., 2015) like increased  $\text{H}_3^+$  densities or elevated temperatures.  $\text{H}_3^+$  molecules might be transported from a copious source in the polar region to mid-to-equatorial latitudes, or directly produced locally through particle precipitation from an inner magnetospheric source. Local Joule heating may be invoked to elevate temperature (Miller et al., 1997). Considerations related to the latitudinal extent of the  $\text{H}_3^+$  emission were used to support the hypothesis that precipitation of magnetospheric charged particles might be responsible for the observed emissions (Morioka et al., 2004; Melin et al., 2006). Temperature measurements at auroral latitudes demonstrated a good correlation with emission brightness (Lam et al., 1997; Stallard et al., 2002; Raynaud et al., 2004; Lystrup et al., 2008; Melin et al., 2006), suggesting that Joule heating is primarily responsible for these emissions. Recent ground-based observations fail to confirm this, since they do not find a clear correlation between the derived temperature,  $\text{H}_3^+$  total emission and column density in the northern auroral region (Johnson et al., 2018). This might rather suggest that in the auroral region the variability of the  $\text{H}_3^+$  emission is more controlled by ionization and ion production rather than temperature variations (Johnson et al., 2018). However, at mid-to-low latitudes,  $\text{H}_3^+$  emission is more likely explained by transport from the auroral regions and/or precipitation of particles with energies on the order of a few keV (Lam et al., 1997).

Several  $\text{H}_3^+$  bands can be observed in the infrared (IR) range, from  $2\ \mu\text{m}$  to  $5\ \mu\text{m}$  (Drossard et al., 1989; Giles et al., 2016). In particular, the  $3\ \mu\text{m}$  spectral region is particularly suitable to study the  $\text{H}_3^+$  emission, as methane absorbs most of the radiation emitted from or scattered by the lower atmosphere of Jupiter (Connerney and Satoh, 2000). When the atmosphere is optically thin, the relative intensity of multiple  $\text{H}_3^+$  IR emission lines can be used to infer  $\text{H}_3^+$  densities and to estimate atmospheric temperatures (e.g. Lam et al., 1997; Stallard et al., 2002), because the  $\text{H}_3^+$  ions quickly thermalize after their formation.

Mid-resolution spectroscopic observations of Jupiter's disc in the  $3.37\text{--}3.57\ \mu\text{m}$  region allowed Miller et al. (1997) to measure the distributions of the  $\text{H}_3^+$  column density and temperature from about  $70^\circ\text{N}$  to  $75^\circ\text{S}$ , along the local noon meridian. Miller et al. (1997) reported a decrease of the  $\text{H}_3^+$  column density from about  $1.0 \times 10^{12}\ \text{cm}^{-2}$  at  $55^\circ$  to  $0.1 \times 10^{12}\ \text{cm}^{-2}$  towards the equator. However, derived temperatures showed a local maximum at auroral latitudes and another close to the equator, with a local minimum at mid latitudes.

Similarly, Ballester et al. (1994), using United Kingdom Infrared Telescope (UKIRT) data, reported the highest temperature measurement ( $1220 \pm 120\ \text{K}$ ) at the equator. Temperature estimates for Northern latitudes ( $734 \pm 37\ \text{K}$ ) were slightly lower than those in the South ( $813 \pm 41\ \text{K}$ ). A recent investigation of the temperature distribution derived from  $\text{H}_3^+$  lines showed an enhancement of temperature at the border of the Great Red Spot (GRS) located northward at  $13^\circ\text{S}$  in lati-

tude with a value of about  $1600\ \text{K}$ . This value is higher than those measured in the auroral region, while temperatures as low as  $800\ \text{K}$  were recorded at the Southern border of the GRS at  $27^\circ\text{S}$  (O'Donoghue et al., 2016), showing a localized thermal process. Acoustic waves are a possible heat source. They are thought to increase temperature of about  $10\ \text{K}$  per day, up to hundreds of K. These measurements highlight the first indirect coupling between lower and upper atmosphere in a giant planet. On the other hand, temperature differences of  $>800\ \text{K}$  at the two latitudes close to the GRS might be due to a  $\text{CH}_4$  contamination at the  $3.45\ \mu\text{m}$ , provided that  $\text{CH}_4$  is more concentrated in the South than in the North.

Recently, observations in the  $5\text{-}\mu\text{m}$  region allowed Giles et al. (2016) to identify several lines of the  $\nu_2$  fundamental and  $2\nu_2(2)\text{-}\nu_2$  hot band of  $\text{H}_3^+$ , which were used to infer the kinetic, rotational and vibrational temperatures in Jupiter's troposphere. These authors reported a kinetic temperature equal to  $1390 \pm 160\ \text{K}$ , in agreement with previous observations of the emission line at  $3.5\ \mu\text{m}$  by Drossard et al. (1989). The rotational temperature, obtained from the relative intensities of 15 different lines of the  $\nu_2$  band, was  $960 \pm 40\ \text{K}$ , while the estimated vibrational temperature was  $925 \pm 25\ \text{K}$ . These results suggest that the assumption of an atmosphere in local thermodynamic equilibrium (LTE) is partially satisfied. However, a significant departure from LTE is to be expected in regions where the atmosphere is hot and tenuous, that is, for altitudes higher than  $\sim 2000\ \text{km}$  above the 1-bar level, as reported by Melin et al. (2005).

To date, observations have not been sufficient to determine the vertical profile of  $\text{H}_3^+$  emission in Jupiter's atmosphere at mid-low latitudes. The first vertical profile was obtained in the auroral region at Southern latitudes, from NIRSPEC spectrometer observations at the Keck II telescope (Lystrup et al., 2008). The authors used an onion peeling technique to derive the vertical profile of the ion densities and temperatures. Ion densities are in fairly good agreement with models (Grodent et al., 2001), for altitudes up to  $1800\ \text{km}$ , while the exospheric temperature was about  $1450\ \text{K}$ ,  $150\ \text{K}$  higher on average than the predicted values. Further vertical emissivity profiles of  $\text{H}_3^+$  were obtained from the InfraRed Camera and Spectrometer (IRCS) at the Subaru 8.2-telescope (Uno et al., 2014). These measurements included lines of the  $\text{H}_3^+$  overtone and hot overtones in the near-infrared, probing the central meridian longitudes (Sys III) equal to  $259^\circ$ ,  $265^\circ$  and  $269^\circ$ , of the North auroral region. Based on the onion peeling technique described in Lystrup et al. (2008), Uno et al. (2014) reported different peak altitudes for the  $\text{H}_3^+$  overtone and hot overtone, respectively located at  $700\text{--}900\ \text{km}$  and  $680\text{--}950\ \text{km}$  above the 1-bar level, and both lower than expected from models (Melin et al., 2005; Grodent et al. 2001). However, the  $\text{H}_3^+$  emissions at auroral and mid-low latitudes might not occur at the same altitude.

From Cassini/VIMS data acquired during the flyby with Jupiter in 2000–2001,  $\text{H}_3^+$  emission at mid-to-low latitudes was estimated to originate between  $300$  and  $500\ \text{km}$  above the 1-bar level (Stallard et al., 2015), according to the current models (Tao et al., 2011).

Juno's unique orbital trajectory affords an opportunity to investigate  $\text{H}_3^+$  emissions from a vantage point very close to Jupiter. In particular, the Jupiter InfraRed Auroral Mapper instrument (JIRAM) has been specifically designed to measure  $\text{H}_3^+$  emissions in the infrared band. In the present study, we analyze mid- and low-latitude spectral images acquired by JIRAM targeting the limb of the planet during the first and fifth perijove passages, which occurred in August 2016 and March 2017. Our aim is to investigate  $\text{H}_3^+$  emissions at mid and low latitudes, and characterize the distribution of the  $\text{H}_3^+$  density and temperature as a function of altitude. The paper is organized as follows: data are described in Section 2 and the method of analysis is presented in Section 3. Results are discussed in Section 4, followed by conclusions in Section 5.

## 2. Data selection

### 2.1. Instrument description

JIRAM (Jupiter InfraRed Auroral Mapper) consists of an imager and a spectrometer, operating in the infrared band (Adriani et al., 2014, 2016). The imaging function is provided by a charged coupled device (CCD) with each half of the image plane covered by two broad-band filters, centered at 3.45 and 4.78  $\mu\text{m}$  (the L and M bands respectively). The spectrometer spans wavelengths in the range 2–5  $\mu\text{m}$  with 336 individual spectral bins with a mean spectral resolution of about 9 nm. In the present work, we only consider data acquired by the spectrometer. The instantaneous field of view of each pixel along the slit is about  $240 \times 240 \mu\text{rad}$ . Considering the spinning motion of the spacecraft, the JIRAM acquisition time frame cannot exceed 30 s, while the integration time for each spectrum on the slit image is 1 s. The internal JIRAM de-spinning mirror compensates for the spacecraft rotation and hence each slit image can be combined to obtain a hyperspectral 3-D image, with the X dimension of the cube corresponding to the cross-track direction (samples), the Y one along the track (lines) and the Z dimension provided by the wavelength (bands). Limb observations are acquired whenever the spectrometer slit is in a suitable configuration; however their location on the planet cannot be planned in advance, due to the limited degrees of freedom of the spacecraft and of the instrument within the spacecraft.

For this work, we used data acquired on 26–27 August 2016 and on 27 March 2017, during the first and fifth perijove passages respectively. During these orbits, JIRAM collected images at a distance of about 500,000–1,200,000 km (7–17  $R_J$ ) from Jupiter, with a spatial resolution ranging from  $\sim 120$  to  $\sim 300$  km per pixel. The limb profiles were selected from the sessions listed in Table 1.

One example of the JIRAM images is shown in Fig. 1, that presents an image acquired on 26 August 2016 at 17:54:19 UT (image name 160,826–175,419). JIRAM slit is made of 256 pixels and each pixel expands into 336 spectral channels, all relative to the same instrumental view. The slit direction is along the X axis, while the Y axis represents the number of slit acquisitions during this image. In this figure, the radiance acquired for the spectral band 172, which corresponds to the wavelength 3.53  $\mu\text{m}$ , where a strong  $\text{H}_3^+$  line is observed, is displayed for a total of 9 slits images. The shaded area marks the region covered by the Jupiter disk below the 1-bar level; all the pixels outside this region show the 3.53  $\mu\text{m}$  signal observed above Jupiter 1-bar surface, in limb geometry, that is the subject of the present investigation.

**Table 1**

List of JIRAM spectrometer images used in this study. Latitude and longitude of the sub-tangent point, the solar local time covered in each image, are also reported, as well as the number of profiles.

Image	Latitude	Longitude	Solar local time	# profiles
160,826–175,419	49–63 N	165–192	13.3–16.8	7
160,826–182,432	50–60 N	147–178	13.3–15.4	7
160,826–185,445	46–62 N	129–156	13.5–16.9	7
160,826–192,427	46–62 N	111–139	13.7–16.5	7
160,826–205,434	45–64 N	57–93	13.5–16.1	8
160,827–175,655	37–44 S	35–61	14.9–16.6	7
160,827–181,219	38–45 S	22–50	14.8–16.6	7
160,827–182,739	38–45 S	11–40	14.6–16.5	7
160,827–184,332	37–46 S	0–31	14.5–16.5	8
160,827–185,854	36–46 S	350–22	14.4–16.5	9
160,827–191,417	36–37 S	337–13	14.3–16.5	9
160,827–192,939	35–47 S	328–2	14.2–16.4	10
160,827–194,430	35–48 S	317–354	14.2–16.5	8
170,327–034221	5S-37 N	258–290	9.6–12.2	22

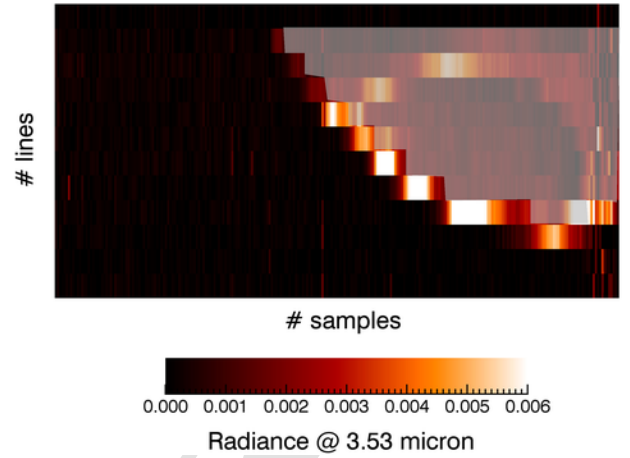


**Fig. 1.** Example of JIRAM image (n. 160,826–175,419) acquired by the spectrometer. The radiance at 3.53  $\mu\text{m}$  is plotted as a function of the samples (pixel) number and lines number. Each line represents one slit acquisition. The shaded area indicates the limit of the Jupiter disk at 1-bar; all pixels outside this region correspond to the  $\text{H}_3^+$  emission originated from regions above the Jupiter disk.

### 2.2. Spectra selection

We searched all the observations of Jupiter's atmosphere acquired by the spectrometer with appropriate limb geometry, i.e., measurements that scanned the atmosphere outside the Jovian disc, to investigate the  $\text{H}_3^+$  emission at mid to low latitudes, with a spatial resolution suitable to investigate the  $\text{H}_3^+$  emission as a function of altitude. We refer to each set of such observations, all belonging to the same slit acquisition, as a 'limb sequence', or 'limb profile'. In the first five orbits that Juno completed around Jupiter, we identified 14 observations that sampled Jupiter limb. These were not the only limb observations available. However, all the other observations including limb measurements acquired during the same Juno orbits, had a spatial resolution too poor to be suitable for this investigation or a poor signal-to-noise ratio that does not allow identifying the  $\text{H}_3^+$  bands. Each limb observation was georeferenced using the tangent altitude, that is the minimum distance between the instrument line of sight (LOS) and the 1-bar surface of Jupiter, and the latitude and longitude of the point where the normal to the LOS at the tangent point crosses the 1-bar level surface.

An example of the geolocation of three limb scan observations from image 160,826–175,419 is reported in Fig. 2. Each sequence of points indicates the latitude and longitude position of the tangent points of one scan in the altitude region 0–1100 km above the 1-bar level. The distance covered by each sequence of points gives an estimation of the portion of atmosphere sampled by the scan, projected on the planet's disc. As it can be seen, the points sequence samples a small region on the planet's disc, justifying the assumption made in the analysis of a uniform atmosphere within each scan.

JIRAM images are georeferenced in System III planetocentric geographical coordinates, and the corresponding geometrical information is calculated for each JIRAM observation, based on the NAIF-SPICE tool (Acton, 1996).

A total of 123 limb profiles were identified in the available images, and used to derive  $\text{H}_3^+$  emission profiles, densities and temperatures, as described in Section 3. The list of the profiles identified in each observation is reported in Table 1, with information on the latitude, longitude and local time ranges covered during each observation. However, eight profiles, distributed in observations 160,826–175,419, 160,826–182,432, 160,826–185,445, 160,826–192,427 and 160,826–205,434, probe latitudes inside the auroral oval. Being outside the scope of the present study, these profiles were discarded from

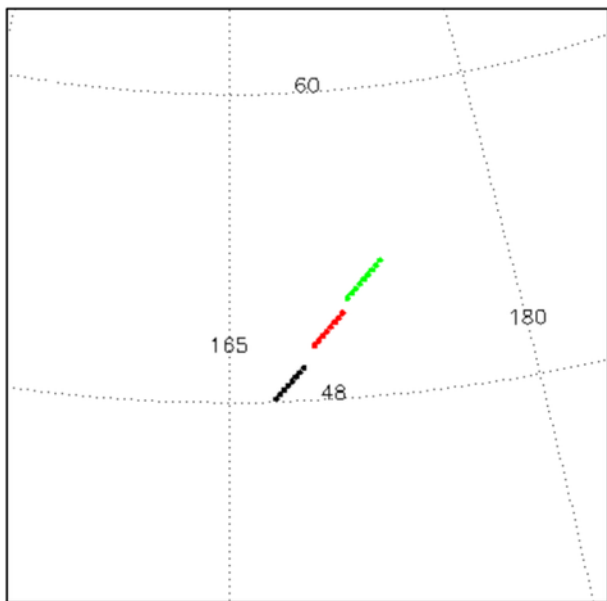


Fig. 2. Horizontal projection of JIRAM observation during the Juno perijove passage 1. The colored points indicate latitude and longitude position of the tangent point in three different limb scans of image 160,826–175,419.

the analysis reducing the number of analyzed profiles to 115, covering the mid and low latitudes.

Within each selected profile, longitude and latitude of the tangent points vary by less than  $1^\circ$ , as shown in Fig. 2. However, it should be noted that in the considered altitude range, which extends approximately from the 1-bar level up to about 1100 km, depending on the geometry observation, the latitude and longitude of the tangent points might vary by up to  $3^\circ$  in total, in the worst case. Finally, it should be recalled that the uncertainty in the spacecraft pointing reconstruction and of the scanning mirror motion, although small, is reflected in the precision on the geometric information, which is correct within 1 pixel.

Assuming that inside a region that extends over  $600 \times 1200$  km in terms of latitude and longitude (calculated for a latitude of  $45^\circ$  at about 200 km above the 1-bar level) there are no horizontal variations in the mixing ratio, it is reasonable to approximate the slant scans to true limb profiles, representing radial variation exclusively.

The selected JIRAM images cover the latitude ranges from  $64^\circ\text{N}$  to  $48^\circ\text{S}$ , albeit unevenly, with one observation (image n. 170,327–034221) encompassing the equator, as reported in Table 1.

Representative examples of JIRAM spectra are shown in Fig. 3 for two different latitudes.  $\text{H}_3^+$  emission lines in the spectral band 3– $3.8\ \mu\text{m}$  can be clearly identified in both spectra, although the intensities in the  $50\text{--}55^\circ\text{N}$  spectrum are about 30% lower than those close to the main auroral oval. These lines are used to derive the density and temperature of the  $\text{H}_3^+$  molecule, as described in Section 3. The feature centred at  $3.8\ \mu\text{m}$  is an artefact due to reflections on the high-order filter on the focal plane of the instrument.

Other  $\text{H}_3^+$  emission lines can be identified at longer wavelengths, but they are not used in this investigation, due to the lower  $\text{CH}_4$  absorption efficiency at these wavelengths, especially at latitudes lower than  $50^\circ$  (Lam et al., 1997). As a consequence, the reflected solar light becomes dominant in the spectra, superimposed to a thermal emission of methane much higher than the background that makes these bands very difficult to be used in a temperature retrieval.

### 3. Method

The selected profiles cover mostly the latitude regions  $30\text{--}50^\circ\text{S}$  and  $45\text{--}64^\circ\text{N}$ , with a few of them observing also part of the main auroral

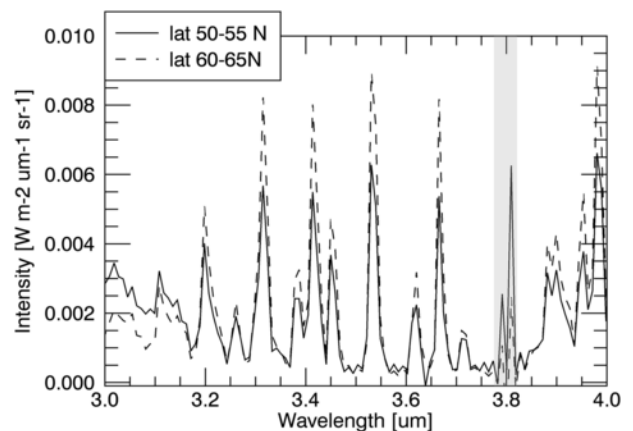


Fig. 3. Averaged spectrum of  $\text{H}_3^+$  emission at  $50\text{--}55^\circ\text{N}$  (solid line) and  $60\text{--}65^\circ\text{N}$  (dashed line), from JIRAM session 160,826–175,419, obtained considering all the pixels with tangent altitudes in the range 0–1100 km above the 1-bar level. The most intense  $\text{H}_3^+$  bands are observed in both spectra at 3– $3.8\ \mu\text{m}$ , although their intensities are on average lower at mid-latitudes. The shaded area identifies an instrumental artefact.

oval in the Northern hemisphere. Some spectra sample the equatorial region. Due to orbital and observational constraints, JIRAM limb spectra could sample only the dayside of Jupiter during the examined perijove passes, with few spectra acquired close to the evening terminator. As a result, we are at present unable to investigate differences between day and night  $\text{H}_3^+$  properties. Data were analyzed neglecting any dependence on Solar Local Time, as the sampling was not sufficient to constrain local time variations. We performed an analysis first on the vertical distribution of the observed  $\text{H}_3^+$  spectrum and then we used the observations to retrieve the vertical distribution of temperature and  $\text{H}_3^+$ .

The retrieval of the vertical variation of temperature and VMR was performed fitting simultaneously all spectra belonging to the same limb sequence. Each pixel of the slit samples the Jupiter atmosphere at several altitudes along the line of sight, the minimum altitudes referred to as the ‘tangent altitude’. The Forward Model (FM) inside the retrieval code numerically solves the radiative transfer integral along the instrument LOS, taking into account both the emission and absorption processes at each sampled atmospheric layer, considering also the finite aperture of the instrument. Jupiter’s atmosphere is assumed perfectly stratified, that is spatially uniform in the horizontal dimension of the plane containing both the instrument LOS and the vertical from the tangent point to Jupiter 1-bar surface, while its composition, pressure and temperature are allowed to vary with the altitude above 1-bar level. The FM is the one already used by Adriani et al. (2011) and García-Comas et al. (2011) to retrieve methane and hydrogen cyanide from their Non-Local Thermal Equilibrium (LTE) emissions in Titan mesosphere.

We assume that the Jovian  $\text{H}_3^+$  emission is in LTE, and therefore that the vibrational and kinetic temperatures coincide. This implies that the retrieved temperatures reported in this paper should be regarded as effective  $\text{H}_3^+$  temperatures. The retrieval is performed using the global fit technique (Carlotti, 1988), that is all the spectra of a limb sequence are simultaneously analyzed to retrieve all the free parameters of the fit, and a Bayesian approach (Optimal estimation, Rodgers, 2000) with an iterative Gauss-Newton procedure.

At each iteration, the solution is given by the following expression:

$$x_{i-1} = x_i + (K^T S_m^{-1} K + S_a^{-1})^{-1} \times [K^T S_m^{-1} \bar{n} - S_a^{-1} (x_i - x_a)]$$

where  $x_i$  is the vector of the solution at iteration  $i$ ,  $K$  is the Jacobian matrix containing the derivatives of the observations with respect to

the retrieved parameters,  $S_m$  is the Variance CoVariance Matrix (VCM) of the measurements,  $x_a$  and  $S_a$  are respectively the a-priori values of the parameters and their VCM, and  $n$  is a vector containing the differences between the observed and the simulated radiances.

The free parameters are: the vertical variation of temperature, the vertical distribution of the  $H_3^+$  Volume Mixing Ratio (VMR), a constant offset and a constant wavelength shift. The offset is retrieved to take into account residual scattering and instrumental effects, while the wavelength shift is retrieved to take into account second order wavelength calibration errors. The same a-priori profiles are used for all the analyses in order to ensure that the observed variability is due to the measurements and not to variable a-priori knowledge. Uncorrelated a-priori errors are assumed to be 100K on temperature and 100% of the a-priori profile for the  $H_3^+$  VMR, with a constant additive bias introduced to avoid strong constraints due to too small a-priori estimates. Despite the differences in the vertical coverage and resolution of the individual limb sequences, we retrieved both T and VMR of  $H_3^+$  on a uniform vertical grid, extending from 200 to 700 km in altitude with 100 km steps. Since the FM does not include the treatment of solar scattering, the retrieval was performed in the spectral region from 3.2 to 3.8  $\mu\text{m}$ , where the spectrum is dominated by the  $H_3^+$  emissions. Spectroscopic data of  $H_3^+$  were taken from the web site <http://h3plus.uuic.edu/database/> (Lindsay and McCall, 2001). During the analyses we observed the contamination by methane emission of the  $H_3^+$  signal in some of the spectra with tangent altitude close to 200 km. This affected the retrieved values of  $H_3^+$  VMR and temperatures, since methane was not included in the FM simulations. Therefore, we decided to discard all the retrieved values at that altitude.

#### 4. Results and discussion

Vertical profiles of the  $H_3^+$  emission, integrated in the 3–3.75  $\mu\text{m}$  spectral band, are shown in Fig. 4. A continuum, estimated at 3  $\mu\text{m}$  and 3.75  $\mu\text{m}$ , outside of the contaminated channels, has been subtracted from the signal. To have a statistically significant number of spectra in each latitude bin, the data were spatially averaged over 10° wide bins. The error bar is calculated as the standard deviation of the data considered in each latitude bin, corrected for the number of data in each bin. A local intensity maximum at 300–400 km above the 1-bar level can be

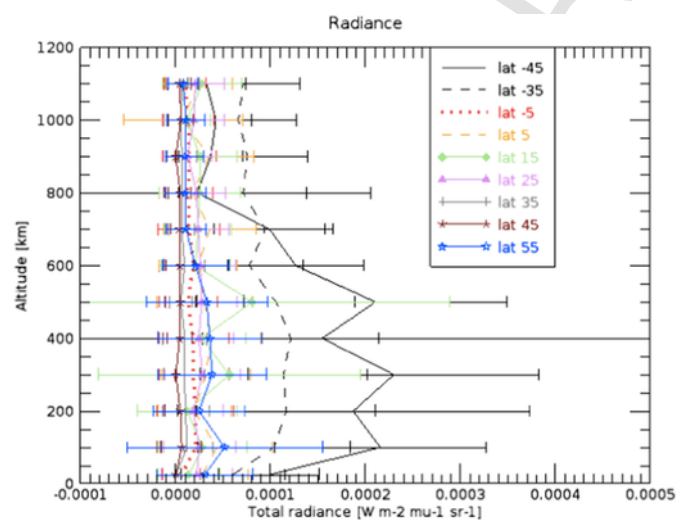


Fig. 4. Vertical profile of  $H_3^+$  emission, integrated in the 3–3.8  $\mu\text{m}$  band. Data are averaged in latitude bins of 10°. Associated errors correspond to the standard deviation corrected for the number of the data in each bin. A local maximum of emission at about 300–400 km is observed at 35° S (dashed black curve), 45° S (solid black curve) and possibly at 55° N (blue curve). No peculiar trend with altitude is observed for other considered latitudes. (For interpretation of the references to colour in this figure legend, the reader is referred to the web version of this article.)

identified in the profiles at 35°S, 45°S and 55°N, while no clear trends are observed in the other analyzed latitude bins. The  $H_3^+$  emission appears to be present at altitudes where methane should prevent the presence of the ion: we attribute this to the intrinsic properties of limb observations. In fact, when observing the atmosphere in limb geometry, the recorded signal is attributed to the tangent altitude of the examined spectrum. Indeed, the optical path in the layer close to the tangent altitude is the one that weights the most. In reality the signal is the result of the emission and absorption processes along the instrument line of sight. Therefore, even if at the tangent altitude of the observation there is no  $H_3^+$ , it is still possible to see its signal in the spectra as a result of the presence of  $H_3^+$  at higher altitudes. This fact prevents the drawing of final conclusions about the  $H_3^+$  vertical distribution just from the observed intensity, and proper radiative transfer calculations are necessary.

Results from the radiative transfer inversion are shown in Fig. 5.

The VMR map shown in Fig. 5a is obtained averaging all the retrieved values in bins of 10 degrees of latitude, as for the emission. The high VMR observed at 700 km at 50–60°N is probably due to auroral contamination in our observations. In Fig. 5a, we see that the  $H_3^+$  VMR values observed in the southern hemisphere are about twice those in the North at nearly all the altitudes for latitudes below 20°S. However, this asymmetry is more evident above 500 km, where the  $H_3^+$  enhancement extends north of the equator. A similar behavior has previously been observed in the auroral region, as reported by Adriani et al. (2017). Although a temperature asymmetry between North and South was reported by Ballester et al. (1994), they were not able to derive a clear conclusion for the  $H_3^+$  VMR. It is worth recalling that our data covering the equatorial region were mainly acquired during the fifth perijove passage due to spacecraft orbital constraints, i.e. seven months apart with respect to the data sampling the mid latitudes. Hence, any observed variability might be due to intrinsic  $H_3^+$  intensity and temperature variability on monthly time scales, as pointed out in Miller et al. (1990).

Fig. 5b reports the map of the  $H_3^+$  concentrations, obtained by combining the retrieved VMRs shown in Fig. 5a and the temperatures shown in Fig. 5c.

Fig. 6 shows that the variability found in the vertical distribution of  $H_3^+$  VMR and concentration is not anti-correlated to a similar variability in the temperature distribution. This suggests that the retrieved values of VMR and temperature are independently determined, provided that the assumed pressure vertical distribution is correct. Here we have considered  $H_3^+$  VMR, concentration and temperature averaged at all considered latitudes.

The  $H_3^+$  concentration values are of the order of  $5 \times 10^4 \text{ cm}^{-3}$  above 300 km, decreasing to about  $2 \times 10^3 \text{ cm}^{-3}$  around 650 km. The distribution of  $H_3^+$  concentration below 300 km increases from the South hemisphere to the North, while an opposite trend is observable in the altitude region from 300 to 400 km. A local minimum is observed at about 300 km around the 10°S latitude and at 400–500 km in the latitude region 10°S–40°N. An increase of the  $H_3^+$  concentration at all the altitudes is observed at latitudes poleward of 60°N, probably due to the fact that the LOS of the instrument at those latitudes is already sampling either the main auroral oval or a region of enhanced emissions equatorward of the main oval and poleward of the Io footprint (Sato et al., 1996; Sato and Connerney, 1999). We assume that the Jovian atmosphere is horizontally homogeneous along the LOS direction in the analysis of each limb sequence, and that the  $H_3^+$  signal is optically thin. Therefore, our retrieval code attributes the auroral contamination of the signal to the tangent altitudes of the measurements, producing an artificial enhancement of the  $H_3^+$  concentrations at all altitudes.

The  $H_3^+$  concentration decrease at 300–400 km from about  $1.4 \times 10^5 \text{ cm}^{-3}$  to  $2 \times 10^4 \text{ cm}^{-3}$ , reported in Fig. 5b, is in partial agree-

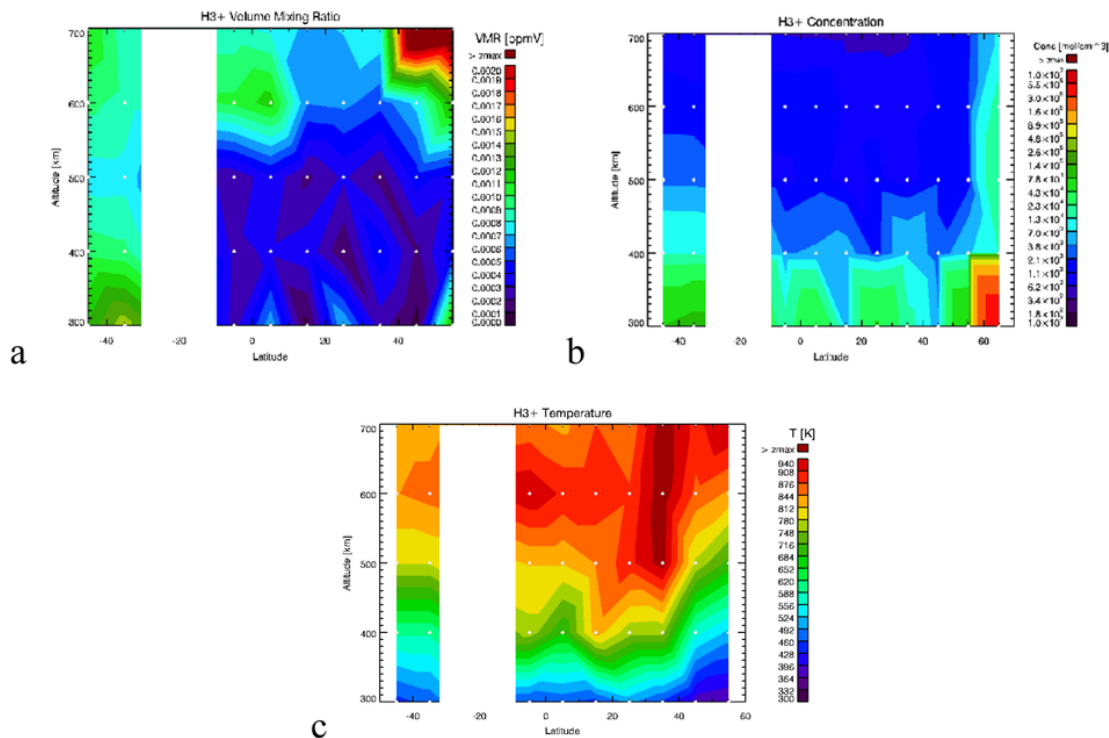


Fig. 5. H<sub>3</sub><sup>+</sup> VMR (a), concentration (b) and temperature (c) maps obtained from the analysis of the limb data in Sys III. White points in the figures indicate the latitude and altitude values of each bin of the considered grid. The white area, instead, indicates a region where no data are available in the considered dataset.

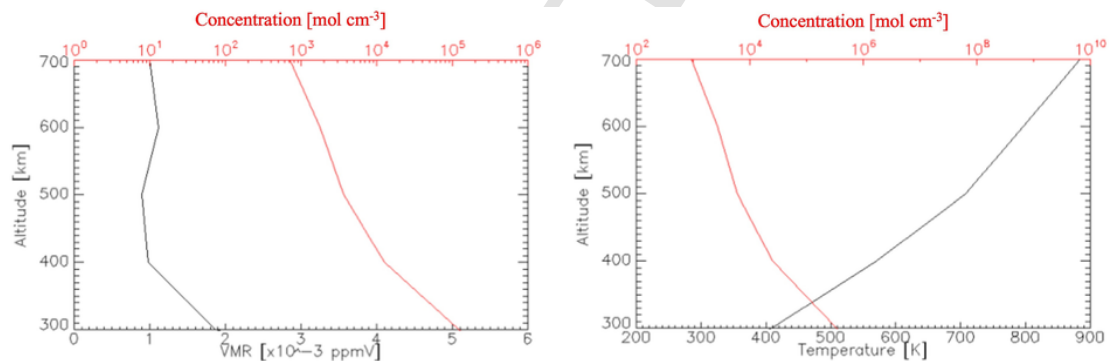


Fig. 6. Correlation of VMR and H<sub>3</sub><sup>+</sup> concentration (image on the left) and between temperature and H<sub>3</sub><sup>+</sup> concentration (image on the right), retrieved with our inversion code. The scale for VMR and temperature are shown in the lower x-axis, while in the upper one there are the values for concentration in log-scale (in red). Data at all available latitudes were averaged. (For interpretation of the references to colour in this figure legend, the reader is referred to the web version of this article.)

ment with the column densities values of Miller et al. (1997), where a decrease of the H<sub>3</sub><sup>+</sup> column density from around 55° ( $1.0 \times 10^{12} \text{ cm}^{-2}$ ) towards the equator (value of  $0.1 \times 10^{12} \text{ cm}^{-2}$ ) was shown.

The retrieved temperatures can be considered representative of the atmospheric temperature, if we assume that the H<sub>3</sub><sup>+</sup> emission is in quasi-LTE. Although this assumption is on average inapplicable, as demonstrated in Melin et al. (2005), it is still a good approximation below 1000 km above the 1-bar level for Jupiter's atmosphere, since major departure from the LTE condition is observed above 2000 km (Melin et al., 2005).

Under these constraints, the map presented in Fig. 5c indicates that the atmospheric temperatures increase from about 400 K to >900 K between 300 km and 700 km. The trend is nearly homogeneous in both hemispheres up to 400 km, while some structures can be identified in the altitude range of 400–700 km. In particular a hot region is observed around 35°N that propagates towards the equatorial region.

In order to point out possible links of temperature with the Jupiter's magnetic field, we calculated its distribution also in System II (see Fig.

7), in which z-axis is oriented along the magnetic dipole. Geometric parameters were derived using appropriate SPICE kernels. No significant variations from one reference system to the other are observed. However, the hot temperature region located at 400–700 km at about 20–30°N, observed in both Fig. 5c and 7, has a more defined structure in the latter. Due to the sparse coverage it is difficult to derive conclusions on possible links with the properties of the magnetic field. This aspect is worth further investigation considering a wider dataset, in a future work.

Localized strong H<sub>3</sub><sup>+</sup> emissions were observed at the borders of the GRS around 27°S, with temperatures on the order of 800 K (O'Donoghue et al., 2016), in a position quite symmetric with respect to the temperature enhancement observed in the JIRAM temperature maps (Fig. 5c). The suggested heating source from the lower atmospheric layers to explain these features involves gravity or acoustic waves. Such heating regions are proof of links between lower and upper atmosphere. Small-scale waves have been frequently observed in the Jupiter's atmosphere at different latitudes and pressure levels (see

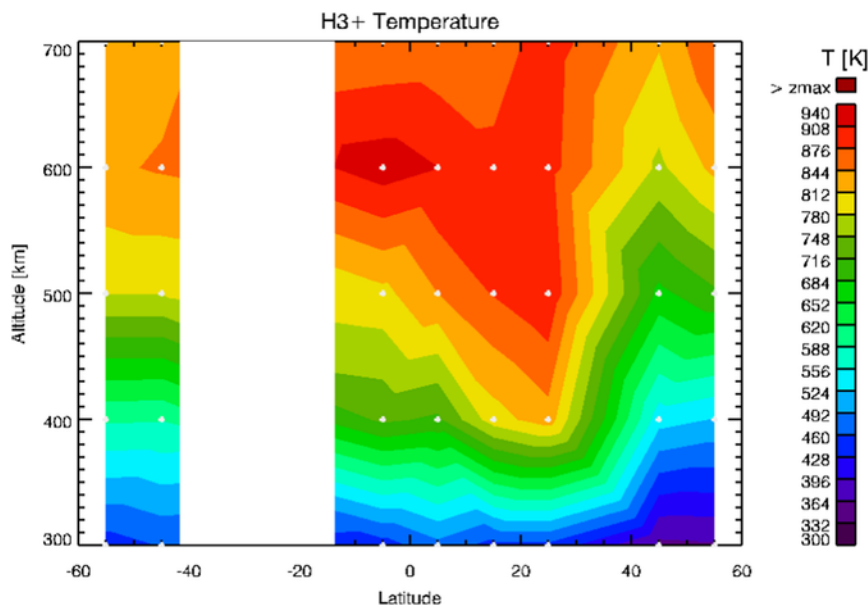


Fig. 7. Temperature map obtained from the analysis of the limb data, projected in terms of Sys II latitude. White points in the figure indicate the latitude and altitude values of each bin of the considered grid. The white area, instead, indicates a region where no data are available in the considered dataset.

for example Simon et al., 2015). Wave structures were also reported in the Northern Equatorial Belt with JIRAM (Adriani et al., 2018), at pressure levels below 1 bar, suggesting that the phenomenon extends across different altitudes. The presence of waves at mid-equatorial latitudes at the  $H_3^+$  emission altitudes might also be a possible candidate to shed light on the observed temperature enhancement in our data; however further analysis is required on this point. On the other hand, although a local-time dependence of the temperature was reported by Miller et al. (1990), it cannot be addressed in this work, because the data acquired during different passages were averaged to increase the signal-to-noise ratio.

In Fig. 8, we show the vertical temperature profiles, obtained as averages in  $10^\circ$  latitude. Average values are in the order of 700–900 K at 500–700 km altitude, quite independent of latitude, in reasonable agreement with estimates from ground-based observations (Moore et al., 2017). In this previous work, the authors analyzed the limb profiles acquired with the Keck telescope at  $20^\circ S$  and  $55^\circ N$ , which are comparable to our dataset.

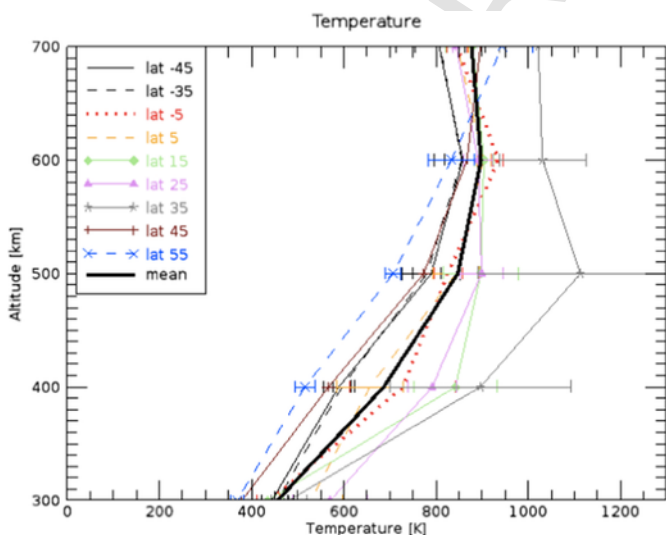


Fig. 8. Vertical profiles of the retrieved  $H_3^+$  temperatures in different latitude bins. A maximum is observed in the 500–600 km region.

Previous complete maps showed temperatures as high as 950 K close to equator and at  $50\text{--}75^\circ S$ , with a patchy distribution (Miller et al., 1997). Local minima were also observed in the Northern hemisphere, showing a quite asymmetric distribution of temperatures with respect to longitude (System III).

A temperature enhancement was reported around the equatorial region between  $30^\circ N$  and  $33^\circ S$  (Ballester et al., 1994), but was not confirmed in Miller et al. (1997). Moreover, temperature values in the Northern hemisphere were on the order of  $734 \pm 37$  K, lower compared to the Southern hemisphere ( $813 \pm 41$  K, Lam et al., 1997). The vertical profiles obtained with the JIRAM data (Fig. 8) indicate a possible enhancement of the temperature around 500 km at  $35^\circ N$ , in partial agreement with Ballester et al. (1994). This seems to contradict; however, the temperatures reported in Miller et al. (1997), where a temperature decrease at  $40^\circ N$  and  $35^\circ S$  was reported.

On the other hand, with our data, we are able to detect an asymmetric VMR distribution between the two hemispheres, but unable to confirm the same trend for the temperature distribution. Different spatial resolutions between the two investigations might be responsible for the observed differences. As shown in previous measurements,  $H_3^+$  column density and derived temperatures present very strong intensities in specific regions locked in System III, when investigated in the mid-low latitudes. Unexpected high values of temperatures and column densities exceeded the predicted values from models, for example, in correspondence of the Great Red Spot (O'Donoghue et al., 2016). Another evidence is reported in Lam et al. (1997) for the auroral emission North/South ratio, which is equal to 2.3 at Central Meridian Longitude (CML)  $160^\circ$ , 10 times stronger than the same value at CML =  $92^\circ$ . Thus, it is important to extend this analysis in order to include additional limb observations and identify possible  $H_3^+$  variability with respect to longitude at the mid-to-low latitudes, to better constrain what was found in previous measurements.

## 5. Conclusions

JIRAM spectra acquired during the early phase of the Juno mission have provided an opportunity to investigate the distribution of the non-auroral  $H_3^+$  emission at mid to low latitudes, resulting in a three-dimensional structure of the stratosphere and thermosphere of Jupiter in

the 60°N–50°S latitude range and between 200 and 700 km above the 1-bar level. Limb observations were used to derive vertical profiles of  $H_3^+$  emission. These measurements are the first to constrain the  $H_3^+$  vertical profile at mid- and low-latitudes, which is of great interest for global circulation models. Since  $H_3^+$  is the dominant ion over most of this region, the electron density is expected to be nearly equal to the ion densities reported here. Their knowledge is essential to calculate the conductivity in the Jovian upper atmosphere, which in turn is a key component to calculate the amount of Joule and ion drag heating sources. Comparison of the observed  $H_3^+$  density distribution with 3-D models will also determine the importance of ionization sources other than solar EUV radiation such as particle precipitation along low magnetospheric L-shells.

The  $H_3^+$  concentration profile shows a quasi-symmetric distribution with latitude, and a decrease from  $5 \times 10^4 \text{ cm}^{-3}$  at 300 km to  $2 \times 10^3 \text{ cm}^{-3}$  at 650 km (which correspond to a column density of  $3.5 \times 10^{12} \text{ cm}^{-2}$  and  $1.4 \times 10^{11} \text{ cm}^{-2}$ , assuming a column depth of 700 km). On the other hand, the  $H_3^+$  mixing ratio is higher in the Southern hemisphere than in the North and temperatures decrease almost monotonically with increasing altitude in both hemispheres.

Intrinsic intensity variability on time scales of days or months could not be investigated, because the spectra were acquired at different times, sampling different regions. Our aim in the present work is to derive the  $H_3^+$  intensity and temperature distribution across the broadest latitudinal region. Moreover, investigation of  $H_3^+$  variability with respect to local time, and in particular day-night variations, was not possible because the spectra were exclusively acquired on the dayside of the planet. Further measurements would be useful to better address the short and long-term variability of  $H_3^+$ . JIRAM is expected to acquire in the future additional spectral data in the limb configuration, especially in the Southern hemisphere.

## Uncited references

Johnson et al., 2017  
Moore et al., 2017

## Acknowledgment

The JIRAM project is funded by the Italian Space Agency (ASI). In particular, this work has been developed under the agreement 2016-23-H.0.

## References

- Acton, C.H., 1996. Planet. Space Sci. Ancillary data services of NASA's navigation and ancillary information facility 44 (1), 65–70. [https://doi.org/10.1016/0032-0633\(95\)00107-7](https://doi.org/10.1016/0032-0633(95)00107-7).
- Adriani, A., Dinelli, B.M., Lopez-Puertas, M., et al., 2011. Icarus, Distribution of HCN in Titan's Upper Atmosphere from Cassini/VIMS Observations at 3  $\mu\text{m}$ . vol. 214, 584–595. <https://doi.org/10.1016/j.icarus.2011.04.016>.
- Adriani, A., Filacchione, G., Di Iorio, T., et al., 2014. JIRAM, the Jovian infrared Auroral mapper. Space Sci. Rev. 213, 393. <https://doi.org/10.1007/s11214-014-0094-y>.
- Adriani, A., Moriconi, M.L., Mura, A., et al., 2016. Juno's earth flyby: the Jovian infrared Auroral mapper preliminary results. Astrophys Space Sci. <https://doi.org/10.1007/s10509-016-2842-9>.
- Adriani, A., Mura, A., Moriconi, M.L., et al., Geophys. Res. Lett., Preliminary JIRAM results from Juno polar observations: 2. Analysis of the Jupiter southern  $H_3^+$  emissions and comparison with the north aurora (2017) 44, doi:<https://doi.org/10.1002/2017GRL072905>.
- Adriani, A., Moriconi, M.L., Altieri, F., et al., The Astrophys. Journal, Characterization of mesoscale waves in the Jupiter NEB by Jupiter InfraRed Auroral Mapper on board Juno (2018) 156, doi:<https://doi.org/10.3847/1538-3881/aae525>.
- Ballester, G.E., Miller, S., Tennyson, J., et al., 1994. Latitudinal temperature variations of Jovian  $H_3^+$ . Icarus 107–189. <https://doi.org/10.1006/icar.1994.1015>.
- Carlotti, M., 1988. Global-fit approach to the analysis of limb-scanning atmospheric measurements. Appl. Opt. 27, 3250–3254.
- Clarke, J.T., Ajello, J., Ballester, G., et al., Nature, Ultraviolet emissions from the magnetic footprints of Io, Ganymede, and Europa on Jupiter (2002) 415–997–(1000).
- Connerney, J.E.P., Satoh, T., 2000. The  $H_3^+$  ion: a remote diagnostic of the Jovian magnetosphere. Phil. Trans. R. Soc. A 358, 2471–2483.

- Connerney, J.E.P., Waite, J.H., 1984. New model of Saturn's ionosphere with an influx of water from the rings. Nature 312, 136–138. <https://doi.org/10.1038/312136a0>.
- Connerney, J.E.P., Baron, R., Satoh, T., Owen, T., 1993. Images of excited  $H_3^+$  at the foot of the Io flux tube in Jupiter's atmosphere. Science 262, 1035–1038.
- Dinelli, B.M., Fabiano, F., Adriani, A., et al., Geophys. Res. Lett., Preliminary JIRAM results from Juno polar observations: 1. Methodology and analysis applied to the Jovian northern polar region (2017) 44, doi:<https://doi.org/10.1002/2017GRL072929>.
- Drossard, P., Maillard, J.-P., Cladwell, S.J., et al., 1989. Detection of  $H_3^+$  on Jupiter. Nature 340, 539–541. <https://doi.org/10.1038/340539a0>.
- García-Comas, M., Lopez-Puertas, M., Funke, B., et al., 2011. Analysis of Titan  $CH_4$  3.3  $\mu\text{m}$  upper atmospheric emission as measured by Cassini/VIMS. Icarus 214, 571–583. <https://doi.org/10.1016/j.icarus.2011.03.020>.
- Gérard, J.-C., Mura, A., Bonfond, B., Gladstone, G.R., Adriani, A., Hue, V., ... Moriconi, M.L., 2018. Concurrent ultraviolet and infrared observations of the north Jovian aurora during Juno's first perijove. Icarus 312, 145–156.
- Giles, R.S., Fletcher, L.N., Irwin, P.G.J., et al., Astron. Astrophys., Detection of  $H_3^+$  auroral emission in Jupiter's 5-micron window (2016) 589: A67, doi:<https://doi.org/10.1051/0004-6361/201628170>.
- Grodent, D., Waite Jr., J.H., Gérard, J.C., 2001. A self-consistent model of the Jovian auroral thermal structure. J. Geophys. Res. 106 (12), 933–12,952. <https://doi.org/10.1029/2000JA900129>.
- Johnson, R.E., Stallard, T.S., Melin, H., Nichols, J.D., 2017. Jupiter's polar ionospheric flows: high resolution mapping of spectral intensity and line-of-sight velocity of  $H_3^+$  ions. J. Geophys. Res. 122, 7599–7618. <https://doi.org/10.1002/2017JA024176>.
- Johnson, R.E., Melin, H., Stallard, T.S., Tao, C., Nichols, J.D., Chowdhury, M.N., 2018. Mapping  $H_3^+$  temperatures in Jupiter's northern auroral ionosphere using VLTR/CRIRES. J. Geophys. Res. 123, 5990–6008. <https://doi.org/10.1029/2018JA025511>.
- Lam, H.A., Achilleos, N., Miller, S., et al., 1997. A baseline spectroscopic study of the infrared auroras of Jupiter. Icarus 127, 379–393.
- Lindsay C. M. and B. J. McCall, J. Mol. Spectrosc., Comprehensive evaluation and compilation of  $H_3^+$  spectroscopy (2001) 60–83, doi:<https://doi.org/10.1006/jmsp.2001.8444>.
- Lystrup, M.B., et al., 2008. First vertical ion density profile in Jupiter's auroral atmosphere: direct observations using the Keck II telescope. Astrophys. J. 677, 790–797. <https://doi.org/10.1086/529509>.
- Melin, H., Miller, S., Stallard, T., Grodent, D., 2005. Non-LTE effects on  $H_3^+$  emission in the Jovian upper atmosphere. Icarus 178, 97–103. <https://doi.org/10.1016/j.icarus.2005.04.016>.
- Melin, H., Miller, S., Stallard, T., et al., 2006. Estimated energy balance in the Jovian upper atmosphere during an auroral heating event. Icarus 181, 256–265. <https://doi.org/10.1016/j.icarus.2005.11.004>.
- Miller, S., Joseph, R.D., Tennyson, J., 1990. Infrared emissions of  $H_3^+$  in the atmosphere of Jupiter in the 2.1 and 4.0 micron region. Astrophys. J. 360, L55–L58.
- Miller, S., Achilleos, N., Ballester, G., et al., 1997. Mid-to-low latitude  $H_3^+$  emission from Jupiter. Icarus 130, 57–67.
- Miller, S., Achilleos, N., Ballester, G., et al., 2000. The role of  $H_3^+$  in planetary atmospheres. Phil. Trans. R. Soc. Lond. A <https://doi.org/10.1098/rsta.2000.0662>.
- Moore, L., O'Donoghue, J., Melin, H. & Stallard, T., EPSC Abstracts, Non-auroral altitude profiles of  $H_3^+$  density and temperature at Jupiter (2017) Vol 11, EPSC2017-285.
- Moore, L., O'Donoghue, J., Müller-Wodarg, I., et al., 2015. Saturn ring rain: model estimates of water influx into Saturn's atmosphere. Icarus 245, 355–366. <https://doi.org/10.1016/j.icarus.2014.08.041>.
- Morioka, A., Yaegashi, S., Nozowa, H., et al., 2004.  $H_3^+$  emissions in the Jovian sub-auroral region and auroral activity. Geophys. Res. Lett. 21, L16806 <https://doi.org/10.1029/2004GL020390>.
- Mura, A., Adriani, F., Altieri, F., et al., 2017. Infrared observations of Jovian aurora from Juno's first orbits: main oval and satellite footprints. Geophys. Res. Lett. 44, <https://doi.org/10.1029/2017GRL072954>.
- Mura, A., Adriani, F., Altieri, F., et al., Science, Juno observations of spot structures and a split tail in Io-induced aurorae on Jupiter (2018), 361, 774–777, doi:<https://doi.org/10.1126/science.aat1450>.
- O'Donoghue, J., Moore, L., Stallard, T.S., Melin, H., 2016. Heating of Jupiter's upper atmosphere above the Great Red Spot. Nature 536, 190–193. <https://doi.org/10.1038/nature18940>.
- Raynaud, E., Lellouch, E., Maillard, J.-P., et al., 2004. Spectro-imaging observations of Jupiter's 2- $\mu\text{m}$  auroral emission. I.  $H_3^+$  distribution and temperature. Icarus 171, 133–152. <https://doi.org/10.1016/j.icarus.2004.04.020>.
- Rodgers, C.D., 2000. Inverse methods for atmospheric sounding: Theory and practice. In: World Scientific, (Singapore).
- Satoh, T., Connerney, J.E.P., 1999. Jupiter's  $H_3^+$  emissions viewed in corrected Jovimagnetic coordinates. Icarus 141, 236–252.
- Satoh, T., Connerney, J.E.P., Baron, R., 1996. Emission source model of Jupiter's  $H_3^+$  aurorae: a generalized inverse analysis of images. Icarus 122, 1–23.
- Simon, A.A., Li, L., Reuter, D.C., 2015. Small-scale waves on Jupiter: a reanalysis of New Horizons, Voyager, and Galileo data. Geophys. Res. Lett. 42, 2612–2618. <https://doi.org/10.1002/2015GL063433>.
- Stallard, T., Miller, S., Millward, G., Joseph, R.D., 2002. On the dynamics of the Jovian ionosphere and thermosphere: II. The measurement of  $H_3^+$  vibrational temperature, column density, and total emission. Icarus 156, 498–514. <https://doi.org/10.1016/icar.2001.6793>.
- Stallard, T.S., Melin, H., Miller, S., et al., 2015. Cassini VIMS observations of  $H_3^+$  emission on the nightside of Jupiter. J. Geophys. Res. Space Physics 120, 6948–6973. <https://doi.org/10.1002/2015JA021097>.
- Stallard, T.S., Burrell, A., Melin, H., et al., 2018. Identification of Jupiter's magnetic equator within  $H_3^+$  ionospheric emission. Nature Astron. 2, 773–777. <https://doi.org/10.1038/s41550-018-0523-z>.
- Tao, C., Badman, S.V., Fujimoto, M., 2011. UV and IR auroral emission model for the outer planets: Jupiter and Saturn comparison. Icarus 213, 581–592. <https://doi.org/10.1016/j.icarus.2011.04.001>.

Uno, T., Yasaba, Y., Tao, C., Sakonoi, T., Kagitani, M., Fujisawa, S., Kita, H., Badman, S.V., 2014. Vertical emissivity profiles of Jupiter's northern  $\text{H}_3^+$  and  $\text{H}_2$  infrared au-

roras observed by Subaru/IRCS. *J. Geophys. Res. Space Physics* 119, 10219–10241. <https://doi.org/10.1002/2014JA020454>.

UNCORRECTED PROOF